Highly Elastic Binders Incorporated with Helical Molecules to Improve the Electrochemical Stability of Black Phosphorous Anode for Sodium Ion Batteries

Hongwei Zhang, Zhisheng Lv, Qinghua Liang, Huarong Xia, Zhiqiang Zhu, Wei Zhang, Xiang Ge, Pei Yuan, Qingyu Yan, Xiaodong Chen**

Dr. H. Zhang, Prof. P. Yuan
National Engineering Research Center of Chemical Fertilizer Catalyst, School of Chemical Engineering, Fuzhou University, Fuzhou 350002, China

Dr. H. Zhang, Z. Lv, Dr. Q. Liang, Dr. H. Xia, Dr. Z. Zhu, Dr. W. Zhang, Dr. X. Ge, Prof. Q. Yan, and Prof. X. Chen
School of Materials Science and Engineering, Nanyang Technological University, 50 Nanyang Avenue, Singapore 639798
Email: alexyan@ntu.edu.sg; chenxd@ntu.edu.sg

Keywords: mechanical properties, elastic polymer, black phosphorus, sodium ion batteries

Abstract

Black phosphorus has aroused grand attention as an attractive anode for sodium ion battery because of its high theoretical capacity. Nevertheless, its practical application is hindered by the large volume expansion, which results in rapid capacity decay. Herein, we report that this challenge can be addressed using an elaborately designed binder for the phosphorus-based electrodes. The incorporation of amylose molecules with helical structures endows the linear polyacrylic acid polymer binders with extraordinary stretchability and elasticity under 400% strain. When it is applied as a binder for black phosphorus-based anode for sodium ion battery, the adhesion between the electrode and the current collector is much stronger (2.95 N) than that of polyvinylidene difluoride (PVDF) binder based one (1.90 N). The electrode delivered a capacity as high as 1280 mAh g^{-1} at 200 mA g^{-1} after 300 cycles, better than the electrode with PVDF binder. Impressively, even after 1000 cycles, the electrode with our binder exhibits capacity retention of 80 %. Our work sheds light on the significance of rational design of effective

binders and provides a new strategy to further improve the electrochemical performance of phosphorus-based materials for batteries application, which can be added on directly to other new electrode materials development strategies.

1. Introduction

Due to the low cost and global abundance of Na resources, sodium ion batteries (SIBs) have been regarded as a promising alternative to lithium ion batteries for large energy storage systems such as smart grids.[1] The key in realizing the practical applications of SIBs lies in the development of high performance electrode materials. Recently, various cathode materials, including phosphates,[2] fluorides,[3] Prussian blue analogues,[4] and Na_xTMO_2(TM=Ni, Mn, Co or mixers)[5] have been reported, which deliver satisfying electrochemical performance for SIBs. Nevertheless, the progress in developing anode materials is sluggish. The sodiation of graphite and silicon, the most widely used and studied anodes in LIBs, are demonstrated to be difficult owing to the much larger ionic size of Na^+ (1.02 Å) than Li^+ (0.76 Å).[6] Although hard and porous carbon,[7] intermetallic alloys[8] and transition metal oxide/sulfide[9] have been investigated as anode materials, they suffer from either a low specific capacity or relatively high working voltage, which undoubtedly compromises the energy density of full cells for practical applications. Therefore, more efforts should be devoted to develop novel anode materials with advanced electrochemical properties for practical SIBs applications.

Phosphorous has attracted tremendous attention as new class of anode materials for SIBs with a high theoretical capacity of 2596 mAh g^{-1} (in the form of Na_3P).[10] Red phosphorous exhibits poor electrical conductivity (~10^{-14} S cm^{-1}) and large volume change (> 400 %) during charge/discharge, resulting in limited rate performance and cycling stability.[11]

Black phosphorous (BP) possesses a similar layered structure as graphite and shows high electrical conductivity of 300 S cm^{-1}, which is more suitable as an electrode material.[12] However, BP experiences sluggish reaction kinetics and large volume expansion (> 300 % upon cycling) during sodiation/desodiation process, leading to low reversible capacity and poor cycling stability. To address these issues, elaborate designs of material structures, such as phosphorene-graphene sandwich, black phosphorus/carbon nanotubes composite, and Poly(3, 4-ethylenedioxythiophene) modified exfoliated few-layer BP (E-BP/PEDOT) composite are undertaken to mitigate the negative impact of BP, thereby achieving enhanced cycling stability and rate capability.[13] Beside these strategies, an effective electrode binder can also endure the volume change of anode materials to a larger extent and lower the rigorous requirement of the active material structures. Many research groups have explored a variety of functional binders including polymers, polysaccharides and their derivatives for those electrode materials with large volume change, mainly focusing on Si anode for LIBs.[14] These functional binders not only enhance the interaction between active materials and current collectors, but also improve the conductivity of electrode as well as buffer the large volume change of Si anode, thereby maintaining the integrity of electrode and improving the electrochemical performance. Although there are a variety of publications on the delicate fabrication of BP based electrode materials, the elaborate design of functional binders for BP has been rarely reported. In fact, effective binders could not only overcome the shortages of active materials to achieve enhanced electrochemical performance, but also improve the active materials loading as well as lower the overall cost of batteries fabrication.

Having noticed that a spring is a mechanical object that tends to recover to its original status once depressed or stretched, herein we hypothesize this property would work to enhance the elasticity of polymer binders with the integration of a spring-like molecules. Amylose (Am), a natural polysaccharide which possesses a helical structure, was covalently bonded with a linear polyacrylic acid (PAA) binder, forming a PAA-Am cross-linked network (**Figure 1**). The incorporation of only 5 wt % amylose into PAA backbone renders the obtained polymer network highly elastic and stretchable. The PAA-Am film can be stretched to 400 % without rupture. When it is applied as a binder for BP-graphene (BP/G) composite anode, PAA-Am shows 50 % higher adhesion ability than the polyvinylidene difluoride (PVDF) binder. Importantly, the PAA-Am based electrode displays a high capacity of 1642 mAh g^{-1} at the current of 200 mA g^{-1}. Moreover, even after 1000 cycles, the electrode exhibits a capacity retention of 80 %, corresponding to a capacity decay of 0.02 % per cycle. For comparison, the PAA or PVDF based electrodes show either lower specific capacity or worst capacity retention. Our work sheds light on the significance of rational design of effective binders and provides a new scalable and low-cost strategy to enhance the SIB performance of phosphorus-based electrode towards practical applications.

2. Results and Discussion

The proposed PAA-Am binder was synthesized through the esterification reaction between carboxylic groups on PAA and hydroxide groups on modified amylose. Supporting Information Figure S1 shows the Fourier transform infrared (FTIR) spectra of obtained binders. PAA show a characteristic peak at 1700 cm^{-1}, which is ascribed to the stretching of C=O on carboxylic groups. Amylose presents a characteristic peak at 1010 – 1030 cm^{-}

[1], corresponding to C–O and C–C stretching vibrations of pyranose ring common to all polysaccharides. This peak is observed for PAA-Am, while not in PAA, suggesting that amylose has been successfully integrated into the PAA-Am binder. Importantly, a shoulder peak at 1730 cm^{-1} appear from the spectra of PAA-Am, indicating that ester bonds formed between PAA and amylose. The viscosity of the binders was shown in **Figure 2**a. The PAA solution possesses viscosity of 198 cP in DMSO with a weight ratio of 2.5 %. The viscosity does not change when PAA and amylose are both dissolved in DMSO without esterification reaction, which is due to the very low viscosity of amylose in DMSO. Importantly, the PAA-Am shows higher viscosity than PAA or physically mixed PAA/Am, suggesting the linear PAA polymer has covalently bonded with amylose to form crosslinking networks. This is consistent with the FTIR characterizations. The mechanical properties of PAA and PAA-Am were further examined quantitatively (Figure 2b). The PAA film ruptures with a strain of ~50 %. On the contrary, the PAA-Am film exhibits a much better stretchability that PAA film. No rupture was observed even the PAA-Am film was stretched to 400 %. Moreover, the PAA-Am film shows excellent reversible elasticity. The hysteresis loop of the stress-strain curves does not change significantly during stretch-recovery cycling tests after the first cycle (Figure 2c). The main network of PAA-Am is formed by covalently crosslinking the linear PAA chains as hard segments and helical amylose molecules as soft segments. The excellent mechanical properties of PAA-Am should be originated from the synergic effect of the cross-linking networks and amylose, where the cross-linking structures mitigate the cleavage of hydrogen bonds within PAA chains and the helical amylose molecules function as “nanosprings” to enhance the elasticity of the binders.

BP/G composites are used to exam the performance of PAA-Am as an anode binder for SIBs applications. The BP/G composites were fabricated through the self-assembly of exfoliated BP nanosheets and graphene layers. The structure and morphology of the BP/G composites were shown in Figures S2. The size of BP nanosheets ranges from several hundreds of nanometers to 2 microns, while the graphene layers have a size larger than 5 microns (Supporting Information Figure S2a and b). After self-assembly, the BP nanosheets deposit on the surface of graphene layers and form a sandwich-like structure, consistent with previous report (Supporting Information Figure S2c and d).[13a] EDS analysis suggests the composite contains P, C, and O elements (Supporting Information Figure S3). The BP/G composites were further studied by Raman spectra (Supporting Information Figure S4). The peaks of graphene layers at 1350 and 1580 cm^{-1} correspond to the characteristic peaks of D band and G band, respectively. Three peaks centered at 360, 437, and 466 cm^{-1} were detected from the exfoliated BP nanosheets, which are related to A^1_g, B_{2g}, and A^2_g modes of BP, respectively. Both peaks from BP and graphene can be identified from the BP/G composites, indicating successful assembly of BP and graphene layers, which is in agreement with the TEM and SEM observation.

The adhesive properties of binders are evaluated using a peel-off test.[15] As shown in **Figure 3**a, the PAA binder displays an average adhesion force of 2.96 N in the BP/G/PAA electrode, higher than that of BP/G/PVDF (1.90 N). The better adhesion of PAA orginates from the abandant carboxyl groups which can form hydrogen bonds with the current collector.[14c] The adhesion of PAA-Am shows a negligible decrease after amylose incorporation, exhibiting an average force of 2.95 N in the BP/G/PAA-Am electrode. The BP/G/PVDF electrode can be easily peeled off from the Cu current collector by Scotch

tape (Figure 3b), while the BP/G/PAA-Am electrodes stick well on Cu current collector. Only a small amount of electrode materials was stripped by the tape from the surface of the BP/G/PAA-Am electrodes, indicating the good adhesion of electrodes with the current collectors. The PAA-Am binder with excellent adhesive properties prevents the delamination of active materials from the current collector, therefore ensuring improved electrochemical performance of electrodes.

The wettability of electrode with electrolyte has a significant influence on the accessibility of electrolyte and diffusion rate of sodium ions. To investigate the impact of the binders on the wettability of the electrodes, we measured the contact angles of the electrodes with different binders with liquid electrolyte ($NaClO_4$ dissolved in EC/DEC with FEC additive). As shown in Figure 3c, the BP/G/PVDF exhibits a contact angle of 12.0 º. Remarkably, the electrolyte spreads out on the BP/G/PAA-Am electrode immediately, suggesting the super wettability of the two electrode with electrolyte. This result reveals the PAA-Am binder is beneficial for the diffusion of electrolyte into electrode, which facilitates the fast transport of sodium ions during electrochemical measurements.

The electrochemical stability of the polymer as an anode binder was investigated by cyclic voltammetry (CV). As shown in Supporting Information Figure S5, the CV curves overlapped well after the 2^{nd} cycle from PVDF and PAA-Am binders, suggesting that both PVDF and PAA-Am are electrochemically inert or under a highly reversible process from 2^{nd} cycle onward between 0.01 and 3.0 V.

The binders' effect on the electrochemical properties of the BP/G composites as SIBs anodes was evaluated using half coin cell configuration. Supporting Information Figure S6a shows the cyclic voltammogram (CV) curve of BP/G/PAA-Am electrode in the

voltage range of 0 – 3 V at a scan rate of 0.2 mV s^{-1}. The peak at 1.1 V in the cathodic scanning can be assigned to the formation of solid electrolyte interface (SEI) caused by the decomposition of EC/DEC/FEC based electrolyte. The peaks at 0.5 V and 0.05 V are associated with the insertion of sodium ions to form Na_xP ($1 \leq x \leq 3$).[16] During the anodic scanning, a peak at 0.7 V is observed, which is resulted from the desodiation of Na_xP product. The first galvanostatic discharge–charge profiles of BP/G/PAA-Am electrode is presented in Supporting Information Figure S6b. Three obvious plateaus can be identified from the discharge curve, corresponding to the formation of SEI and Na_xP. The flat plateau at 0.6 V in the charge curve is related to the desodiation of Na_xP. These results are in agreement with the observation in the CV curves and previous literature reports.[16-17]

The cycling performance of the BP/G electrodes with different binders for SIBs was measured at a constant current of 200 mA g^{-1}. As shown in **Figure 4**a, initial discharge capacities of 2524, 2578, and 2526 mAh g^{-1} were delivered for the BP/G/PVDF, BP/G/PAA, and BP/G/PAA-Am electrodes, respectively, which are close to the theoretical capacity (2596 mAh g^{-1}) of BP. The initial Coulombic efficiency of the BP/G/PAA-Am electrode is 61.3 %, much higher than that of BP/G/PVDF (40.5 %) or BP/G/PAA (42.0 %) electrodes. The capacity loss in the first cycle could be attributed to the irreversible decomposition of electrolyte to form SEI films, which is a common phenomenon for battery anodes in the first cycle. The Coulombic efficiency of the BP/G/PAA-Am electrode dramatically increases to 93.5 % in the second cycle, and maintains > 98 % from the tenth cycle onward. Impressively, a capacity as high as 1280 mAh g^{-1} could be reserved for the BP/G/PAA-Am electrode after 300 cycles, much better than the BP/G/PAA (587 mAh g^{-1} after 300 cycles) and the BP/G/PVDF electrode (280 mAh g^{-1} after 150 cycles). The

electrochemical impedance spectra (EIS) of the three electrodes after cycling test were conducted and the Nyquist plots are shown in Figure 4b. The semicircle in the middle frequency is related to the charge transfer resistance (R_{ct}) between the electrolyte and the electrodes, while the plots in low frequency represent the Warburg resistance (Z_W) associated with the Na ion diffusion inside the electrode materials. The R_{ct} of the BP/G/PVDF, BP/G/PAA, and BP/G/PAA-Am electrodes are determined to be 155, 91, and 75 Ω, respectively, based on the fitted equivalent circuit in the inset of Figure 4b. The smaller resistance of the BP/G/PAA-Am electrode indicates a more stable interface and better electrons/ions diffusion of the electrode, which further reveal the significance of PAA-Am binder on improving the interfacial stability and maintain electrical contact between active materials and conductive agents/current collectors.

The rate capability of the BP/G/PAA-Am electrode was further investigated by cycling at various current densities ranging from 0.2–6 A g^{-1} (Figure 4c). BP/G/PAA-Am delivers a high reversible capacity of ~1513 mAh g^{-1} (average for 10 cycles) at 0.2 A g^{-1}. As the current density increases, the capacity decreases gradually. At a high current density of 6 A g^{-1}, an average capacity of 551 mAh g^{-1} can still be reserved. Remarkably, BP/G/PAA-Am exhibits extraordinary cycling stability. A capacity retention of 80 % can be attained even after 1000 cycles at the current of 2 A g^{-1} (Figure 4d). This cycling stability is the best among the reported phosphrous-based eleectrodes for sodium ion batteries (Table S1). The superior electrochemical performance of the BP/G/PAA-Am electrode arises from the PAA-Am binder with excellent stretchability, elasticity and adhesion property, which is beneficial for buffering the large volume change of BP and maintaining the integrity of electrode as well as stabilizing the SEI formation.

The cross section of the electrodes after 50 cycles (in desodiation status) were further investigated by SEM to reveal the difference of electrode thickness change. As shown in **Figure 5**, the thickness of the BP/G/PVDF electrode increased from 8 um to 15.1 um after cycling, suggesting the ineffectiveness of PVDF in mitigating the volume expansion of BP. PAA can partially buffer the volume change, giving an increase of thickness from 8.2 um to 10.5 um. The significant thickness increase of the BP/G/PVDF and BP/G/PAA electrodes arise from volume expansion of BP and repeated SEI formation, which results in delamination and loss of active materials from the current collectors and eventually leads to continuous capacity fading. Impressively, only a slight increase of thickness of the BP/G/PAA-Am electrode (from 8.3 um to 8.8 um) is observed, indicating the highly stretchable and elastic PAA-Am binder is effective in buffering the large volume change of BP and maintaining the integrity of electrode. The coin cells with BP/G/PVDF and BP/G/PAA-Am electrodes after cycling tests was also dissembled and the electrodes were immersed in an EC/DEC solution. As shown in Supporting Information Figure S7, after slight shaking, the electrode structure of BP/G/PVDF degraded rapidly and a large amount of active materials fell off from the current collector. In contrast, the structure of the BP/G/PAA-Am electrode reserved very well. No obvious delamination of active materials from the current collector is observed. This result further proved the excellent mechanical properties of PAA-Am in terms of good adhesion, high stretchability and elasticity, which is responsible for the enhanced electrochemical performance of BP/G composites. Our work sheds light on the effectiveness of designing functional binders with unique mechanical properties in addressing the intrinsic drawbacks of phosphorus with large volume expansion as electrode materials for SIBs applications.

3. Conclusion

In summary, we have developed a novel functional binder via the incorporation of a helical molecule onto PAA to form a cross-linking polymer network. Comparing with the conventional PVDF binder, the PAA-Am binder exhibits not only higher stretchability, but also better adhesion towards BP/G electrodes. The PAA-Am binder endows the electrode with superior electrolyte wettability, thereby imparting the BP/G/PAA-Am electrodes better rate capability than BP/G/PVDF electrodes. Importantly, PAA-Am is able to buffer the large volume change of BP during sodiation/desodiation process and maintain the integrity of the electrode, eventually ensuring good cycling stability. Our work has provided a new strategy to address the challenge of BP anodes with large volume expansion and paved the way for the practical application of BP anodes in SIBs applications.

4. Experimental section

Synthesis of PAA-Am binder

Amylose (0.2 g) was dissolved in aqueous NaOH (200 mL, 1 M) at room temperature by stirring. Propylene oxide (20 mL) was added dropwise and the mixture was keep stirring for 12 h. The solution was then purified by dialysis against deionized H_2O for 3 days and lyophilized to obtain modified amylose.

PAA-Am was prepared through the esterification between commercial PAA and modified amylose. The solutions of PAA (0.05 g mL^{-1}), CDI (0.1 g mL^{-1}) and modified amylose (0.1 g mL^{-1}) were first prepared using anhydrous DMSO as the solvent. PAA (19 mL) and CDI solutions (0.113 mL) were mixed in a round-bottom flask at room temperature and stirred at 50 ºC for 12 h under Ar atmosphere. The solution was then cooled down to room

temperature followed by the addition of modified amylose solution (0.5 mL). After stirring for 10 min, the temperature was increased to 70 ºC and the solution was kept stirring for 72 h. The resulting PAA-Am polymer was precipitated from THF and centrifuged. The collected product was dissolved in MeOH, precipitated from diethyl ether, and centrifuged. The PAA-Am was re-dissolved in deionized water and lyophilized to yield a white polymer. The polymer was dissolved in DMSO with a concentration of 5 wt % for further use and characterizations.

Preparation of BP/G composites

Exfoliated BP and graphene layers were prepared through a liquid-phase exfoliation method. Briefly, BP crystals (20 mg) were ground with the mortar and pestle in with formamide (1 mL) for 20 min. The mixture was transferred to a glass bottle containing 50 mL of formamide. After bubbled with argon for 20 min and careful sealing with parafilm, the glass bottle was sonicated in an ice bath for 6 h. After sonication, the mixture was centrifuged at 4000 rpm for 10 min to remove aggregates and obtain the supernatant. Graphite (50 mg) was also dispersed in formamide (50 mL) and sonicated in a sonic bath for 3 h. The resultant dispersion of graphene was centrifuged at 500 rpm for 30 min to remove sediment and obtain the supernatant. The concentration of exfoliated BP and graphene nanosheets in the supernatants were determined to be 0.18 and 0.11 mg mL^{-1} by weighing the rest sediments after drying.

The exfoliated BP and graphene supernatants were mixed at a fixed ratio, making the weight ratio of BP: graphene be 3: 1. The mixed solution was stirring at room temperature for 6 h, followed by filtration. The self-assembly between exfoliated BP and graphene nanosheets yield sandwich-like BP/G composites during filtration.

Mechanical testing of different polymers (PVDF, PAA, and PAA-Am)

The tensile experiments were conducted on a mechanical tester (MTS C42). The polymer films were prepared by drying the polymer solutions on glass petri dishes at 70 ºC in a vacuum oven. The films were cut into strips with 10 mm width * 40 mm length. The specimens were soaked in electrolyte (1 M $NaClO_4$ in EC/DEC with 5 % FEC) for 6 h before the tensile experiments. The tensile tests were carried out at a strain rate of 3 mm min-1. For dynamic mechanical tests, tensile tests were repeated with the strain of 100 % for 5 times. Adhesion measurements of electrodes with different binders were also performed on the mechanical testor. A Scotch Magic® tape was firmly applied onto the electrode laminate side. The ends of the tape and electrode (the same direction) were fixed to the top and bottom sample holders, respectively. The tape was peeled off from the electrode by moving up the top sample holder at a rate of 5 mm min^{-1}.

Materials characterizations

The composition and structure of obtained PAA-Am were analyzed by Fourier-transform infrared spectroscopy (FTIR) using FT-Raman Spectrometer & IR Microscope (Thermo Scientific). The viscosity of polymer solutions were measured on a Rheometer (Brookfield). The morphology and microstructure of the BP/G composites were investigated by field emission scanning electronic microscopy (FESEM, JEOL JSM-7600F) and TEM (JEOL, JEM-2010). Raman spectra were recorded on a 532 nm micro-Raman spectrometer.

Electrochemical measurements

The electrode slurries were prepared by mixing BP/G composites, conductive agent (Super P) and binders (PVDF, PAA, and PAA-Am) with the ratio of 8: 1: 1. Then the slurry was

coated onto a copper foil and dried at 60 °C for 12 h under vacuum. Coin cells (2032) were assembled in an argon-filled glovebox with concentrations of moisture and oxygen below 0.1 ppm. Sodium metal chips were used as the counter/reference electrode and Whatman GF/D microfiber filter papers were used as the separator. The electrolyte is 1 M $NaClO_4$ dissolved in ethylene carbonate (EC)/ diethyl carbonate (DEC) (1: 1 by volume) with 5% fluoroethylene carbonate (FEC). The galvanostatic charge-discharge tests were recorded on a Neware battery tester in a voltage window of 0.01–3.0 V. Cyclic voltammetry and electrochemical impedance spectroscopy (EIS) were performed on Solatron electrochemical workstation.

Supporting Information

Supporting Information is available from the Wiley Online Library or from the author.

Acknowledgement

The authors gratefully acknowledge the financial supports from the National Natural Science Foundation of China (grants 21776048), Fujian Province Natural Science Funds for Distinguished Young Scholar (2018J06002), Singapore MOE AcRF Tier 1 Grant Nos. RG113/15 and 2016-T1-002-065, and Tier 2 under Grant Nos. 2017-T2-2-069 and 2018-T2-01-010, Singapore EMA project EIRP 12/NRF2015EWT-EIRP002-008 and National Research Foundation of Singapore (NRF) Investigatorship, award Number NRF2016NRF-NRFI001-22. The authors greatly thank the Facility for Analysis, Characterization, Testing and Simulation (FACTS) of Nanyang Technological University, Singapore, for using their TEM, SEM, and XRD equipment.

Received: ((will be filled in by the editorial staff))
Revised: ((will be filled in by the editorial staff))
Published online: ((will be filled in by the editorial staff))

References

[1] a) S. W. Kim, D. H. Seo, X. H. Ma, G. Ceder, K. Kang, *Adv. Energy Mater.* **2012**, *2*, 710; b) M. D. Slater, D. Kim, E. Lee, C. S. Johnson, *Adv. Funct. Mater.* **2013**, *23*, 947; c) V. Palomares, P. Serras, I. Villaluenga, K. B. Hueso, J. Carretero-Gonzalez, T. Rojo, *Energy Environ. Sci.* **2012**, *5*, 5884; d) J. Q. Deng, W. B. Luo, S. L. Chou, H. K. Liu, S. X. Dou, *Adv. Energy Mater.* **2018**, *8,* 1701428.

[2] a) Y. Jiang, Z. Z. Yang, W. H. Li, L. C. Zeng, F. S. Pan, M. Wang, X. Wei, G. T. Hu, L. Gu, Y. Yu, *Adv. Energy Mater.* **2015**, *5*, 1402104; b) J. Kim, D. H. Seo, H. Kim, I. Park, J. K. Yoo, S. K. Jung, Y. U. Park, W. A. Goddard, K. Kang, *Energy Environ. Sci.* **2015**, *8*, 540; c) J. Liu, K. Tang, K. Song, P. A. van Aken, Y. Yu, J. Maier, *Nanoscale* **2014**, *6*, 5081; d) Z. Jian, Y. Sun, X. Ji, *Chem. Commun.* **2015**, *51*, 6381; e) W. Duan, Z. Zhu, H. Li, Z. Hu, K. Zhang, F. Cheng, J. Chen, *J. Mater. Chem. A* **2014**, *2*, 8668.

[3] A. Kitajou, H. Komatsu, K. Chihara, I. D. Gocheva, S. Okada, J. Yamaki, *J. Power Sources* **2012**, *198*, 389.

[4] a) L. Wang, Y. H. Lu, J. Liu, M. W. Xu, J. G. Cheng, D. W. Zhang, J. B. Goodenough, *Angew. Chem. Int. Edit.* **2013**, *52*, 1964; b) H. W. Lee, R. Y. Wang, M. Pasta, S. W. Lee, N. Liu, Y. Cui, *Nat. Commun.* **2014**, *5*, 5280.

[5] a) N. Yabuuchi, M. Kajiyama, J. Iwatate, H. Nishikawa, S. Hitomi, R. Okuyama, R. Usui, Y. Yamada, S. Komaba, *Nat. Mater.* **2012**, *11*, 512; b) X. D. Xiang, K. Zhang, J. Chen, *Adv. Mater.* **2015**, *27*, 5343.

[6] a) R. D. Shannon, *Acta Cryst.* **1976**, *32*, 751; b) V. L. Chevrier, G. Ceder, *J. Electrochem. Soc.* **2011**, *158*, A1011; c) V. V. Kulish, O. I. Malyi, M. F. Ng, Z. Chen, S. Manzhos, P. Wu, *Phys. Chem. Chem. Phys.* **2014**, *16*, 4260.

[7] a) D. A. Stevens, J. R. Dahn, *J. Electrochem. Soc.* **2000**, *147*, 1271; b) D. A. Stevens, J. R. Dahn, *J. Electrochem. Soc.* **2001**, *148*, A803; c) X. H. Yao, Y. J. Ke, W. H. Ren, X. P. Wang, F. Y. Xiong, W. Yang, M. S. Qin, Q. Li, L. Q. Mai, *Adv. Energy Mater.* **2019**, *9*, 1803260; d) S. Wenzel, T. Hara, J. Janek, P. Adelhelm, *Energy Environ. Sci.* **2011**, *4*, 3342.

[8] a) Y. H. Xu, Y. J. Zhu, Y. H. Liu, C. S. Wang, *Adv. Energy Mater.* **2013**, *3*, 128; b) M. M. Lao, Y. Zhang, W. B. Luo, Q. Y. Yan, W. P. Sun, S. X. Dou, *Adv. Mater.* **2017**, *29*, 1700622; c) L. Li, Y. Zheng, S. L. Zhang, J. P. Yang, Z. P. Shao, Z. P. Guo, *Energy Environ. Sci.* **2018**, *11*, 2310; d) W. Luo, F. Li, J. J. Gaumet, P. Magri, S. Diliberto, L. Zhou, L. Q. Mai, *Adv. Energy Mater.* **2018**, *8*, 1703237.

[9] a) Y. P. Zhou, W. P. Sun, X. H. Rui, Y. Zhou, W. J. Ng, Q. Y. Yan, E. Fong, *Nano Energy* **2016**, *21*, 71; b) W. P. Sun, X. H. Rui, D. Yang, Z. Q. Sun, B. Li, W. Y. Zhang, Y. Zong, S. Madhavi, S. X. Dou, Q. Y. Yan, *ACS Nano* **2015**, *9*, 11371; c) Y. H. Liu, X. Y. Yu, Y. J. Fang, X. S. Zhu, J. C. Bao, X. S. Zhou, X. W. Lou, *Joule* **2018**, *2*, 725; d) D. W. Su, S. X. Dou, G. X. Wang, *Adv. Energy Mater.* **2015**, *5*, 1401205.

[10] a) J. F. Ni, L. Li, J. Lu, *ACS Energy Lett.* **2018**, *3*, 1137; b) Y. Q. Fu, Q. L. Wei, G. X. Zhang, S. H. Sun, *Adv. Energy Mater.* **2018**, *8*; c) W. L. Liu, H. Q. Zhi, X. B. Yu, *Energy Storage Mater.* **2019**, *16*, 290.

[11] a) Y. Kim, Y. Park, A. Choi, N. S. Choi, J. Kim, J. Lee, J. H. Ryu, S. M. Oh, K. T. Lee, *Adv. Mater.* **2013**, *25*, 3045; b) W. H. Li, S. H. Hu, X. Y. Luo, Z. L. Li, X. Z. Sun, M. S. Li, F. F. Liu, Y. Yu, *Adv. Mater.* **2017**, *29*, 1605820; c) Z. X. Yu, J. X. Song, D. W.

Wang, D. H. Wang, *Nano Energy* **2017**, *40*, 550; d) X. Z. Sun, W. H. Li, X. W. Zhong, Y. Yu, *Energy Storage Mater.* **2017**, *9*, 112.

[12] a) S. X. Wu, K. S. Hui, K. N. Hui, *Adv. Sci.* **2018**, *5*, 1700491; b) H. W. Liu, K. Hu, D. F. Yan, R. Chen, Y. Q. Zou, H. B. Liu, S. Y. Wang, *Adv. Mater.* **2018**, *30*, 1800295.

[13] a) J. Sun, H. W. Lee, M. Pasta, H. T. Yuan, G. Y. Zheng, Y. M. Sun, Y. Z. Li, Y. Cui, *Nat. Nanotechnol.* **2015**, *10*, 980; b) G. L. Xu, Z. H. Chen, G. M. Zhong, Y. Z. Liu, Y. Yang, T. Y. Ma, Y. Ren, X. B. Zuo, X. H. Wu, X. Y. Zhang, K. Amine, *Nano Lett.* **2016**, *16*, 3955; c) Y. Zhang, W. P. Sun, Z. Z. Luo, Y. Zheng, Z. W. Yu, D. Zhang, J. Yang, H. T. Tan, J. X. Zhu, X. L. Wang, Q. Y. Yan, S. X. Dou, *Nano Energy* **2017**, *40*, 576.

[14] a) I. Kovalenko, B. Zdyrko, A. Magasinski, B. Hertzberg, Z. Milicev, R. Burtovyy, I. Luzinov, G. Yushin, *Science* **2011**, *334*, 75; b) C. Wang, H. Wu, Z. Chen, M. T. McDowell, Y. Cui, Z. A. Bao, *Nat. Chem.* **2013**, *5*, 1042; c) A. Magasinski, B. Zdyrko, I. Kovalenko, B. Hertzberg, R. Burtovyy, C. F. Huebner, T. F. Fuller, I. Luzinov, G. Yushin, *Acs Appl Mater Inter* **2010**, *2*, 3004; d) S. Choi, T. W. Kwon, A. Coskun, J. W. Choi, *Science* **2017**, *357*, 279; e) T. M. Higgins, S. H. Park, P. J. King, C. Zhang, N. McEvoy, N. C. Berner, D. Daly, A. Shmeliov, U. Khan, G. Duesberg, V. Nicolosi, J. N. Coleman, *ACS Nano* **2016**, *10*, 3702.

[15] D. Liu, Y. Zhao, R. Tan, L.-L. Tian, Y. Liu, H. Chen, F. Pan, *Nano Energy* **2017**, *36*, 206.

[16] H. W. Liu, L. Tao, Y. Q. Zhang, C. Xie, P. Zhou, H. B. Liu, R. Chen, S. Y. Wang, *ACS Appl. Mater. Inter.* **2017**, *9*, 36849.

[17] M. Y. Li, N. Muralidharan, K. Moyer, C. L. Pint, *Nanoscale* **2018**, *10*, 10443.

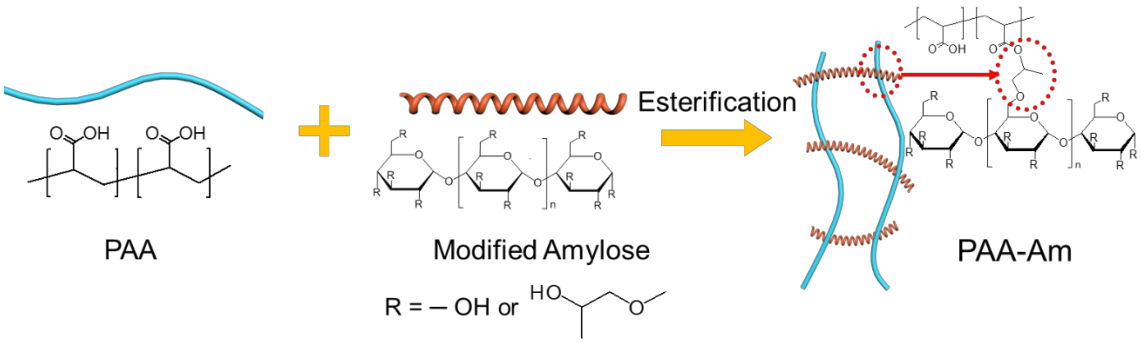

Figure 1. Schematic illustration of the preparation process for PAA-Am binder.

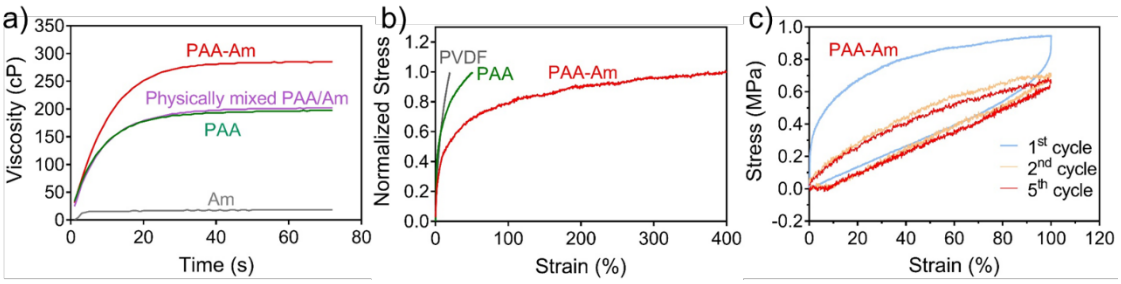

Figure 2. Viscosity of amylose, PAA and PAA-Am (a), comparison of the mechanical properties of PVDF, PAA and PAA-Am films (b), and the stress-strain curves of PAA-Am for 5 stretch-recovery cycles with the strain of 100 % (c).

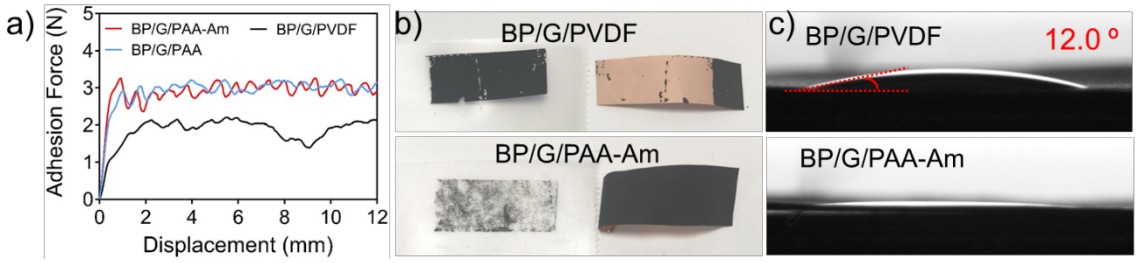

Figure 3. The peel-off tests (a) BP/G/PVDF, BP/G/PAA, and BP/G/PAA-Am electrodes, digital images (b) after peel-off tests and contact angle tests (c) of the BP/G/PVDF and BP/G/PAA-Am electrodes.

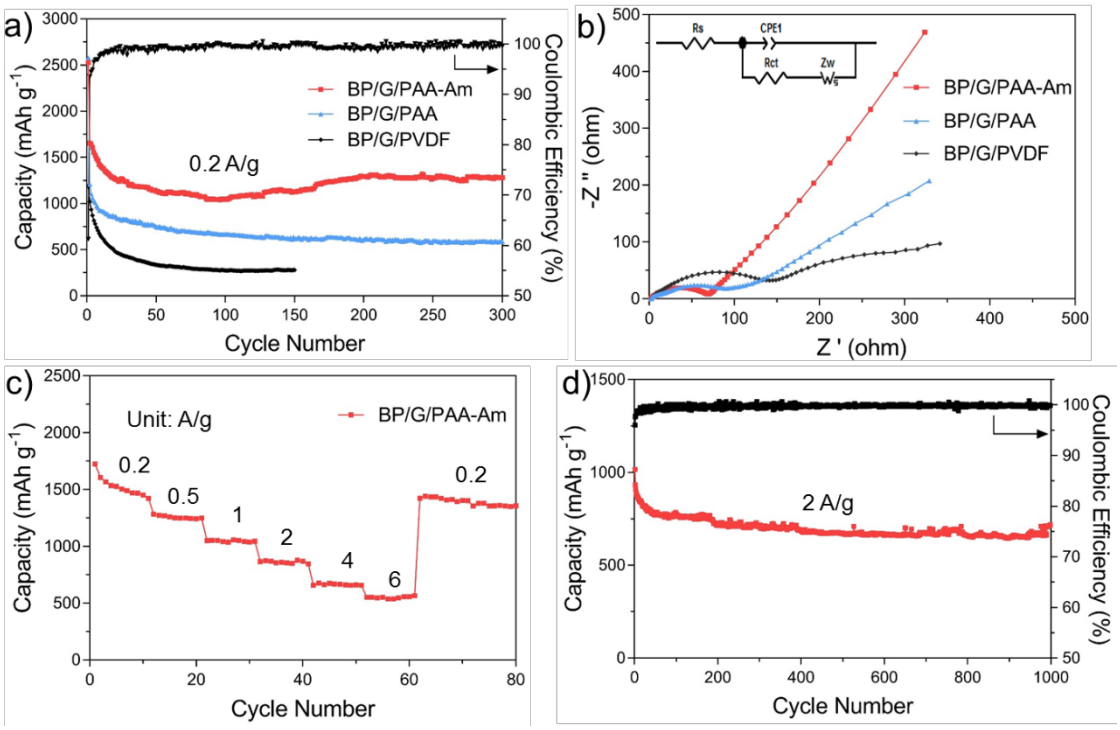

Figure 4. Cycling performance at 0.2 A g^{-1} (a) and Nyquist plots (b) of three electrodes with different binders, rate capability (c) and long-term cycling stability at 2 A g^{-1} (d) of the BP/G/PAA-Am electrode.

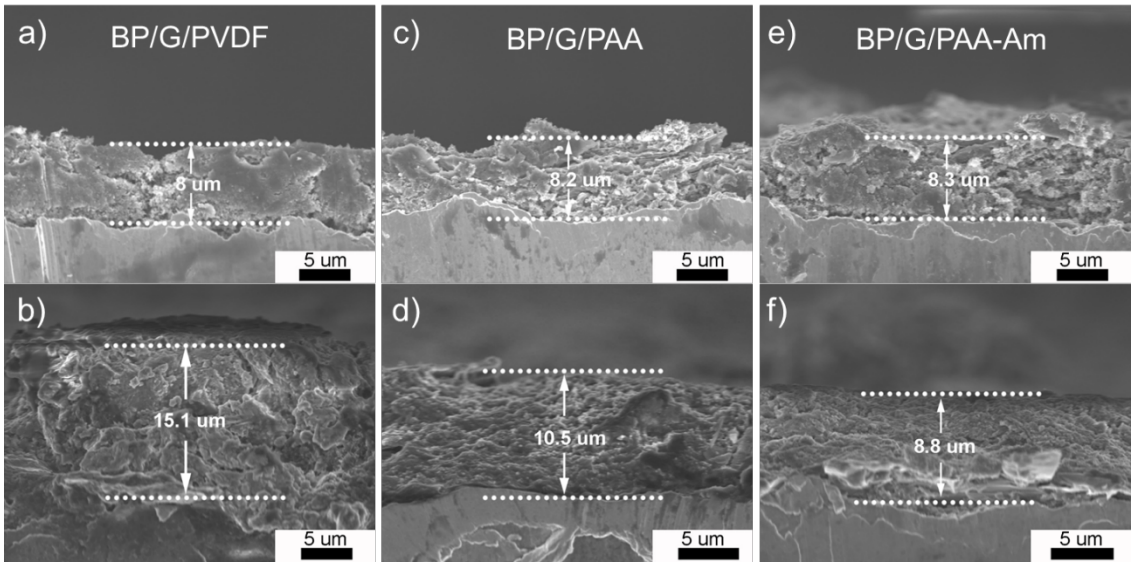

Figure 5. SEM images of cross section of the electrodes with different binders before and after cycling: BP/G/PVDF (a and b), BP/G/PAA (c and d), and BP/G/PAA-Am (e and f).

We have developed a highly elastic polymer via the integration of a helical molecule onto polyacrylic acid. The obtained polymer is able to stretch to 400 % without rapture and recovery to its original state easily. The polymer can buffer the large volume change of phosphorus based electrode, showing significantly improved cycling stability for sodium ion batteries.

Keyword

Dr. H. Zhang, Z. Lv, Dr. Q. Liang, Dr. H. Xia, Dr. Z. Zhu, Dr. W. Zhang, Dr. X. Ge, Prof. P. Yuan, Prof. Q. Yan,* and Prof. X. Chen*

Highly Elastic Binders Incorporated with Helical Molecules Improving the Electrochemical Stability of Black Phosphorous Anode for Sodium Ion Batteries